# Soft Matter

Accepted Manuscript


This is an *Accepted Manuscript*, which has been through the Royal Society of Chemistry peer review process and has been accepted for publication.

*Accepted Manuscripts* are published online shortly after acceptance, before technical editing, formatting and proof reading. Using this free service, authors can make their results available to the community, in citable form, before we publish the edited article. We will replace this *Accepted Manuscript* with the edited and formatted *Advance Article* as soon as it is available.

You can find more information about *Accepted Manuscripts* in the Information for Authors.

Please note that technical editing may introduce minor changes to the text and/or graphics, which may alter content. The journal's standard Terms & Conditions and the Ethical guidelines still apply. In no event shall the Royal Society of Chemistry be held responsible for any errors or omissions in this *Accepted Manuscript* or any consequences arising from the use of any information it contains.

ROYAL SOCIETY OF CHEMISTRY

www.rsc.org/softmatter

ARTICLE TYPE www. rsc.org/xxxxxx | XXXXXXXX

# Phase Behavior of Electrostatically Complexed Polyelectrolyte Gels Using an Embedded Fluctuation Model†

**Debra J. Audus[a,b,‡], Jeffrey D. Gopez[a,b], Daniel V. Krogstad[a,c,x], Nathaniel A. Lynd[a,¶], Edward J. Kramer[a,b,c], Craig J. Hawker[a,c,d], Glenn H. Fredrickson[*a,b,c]**

***Received Xth XXXXXXXXXX 20XX, Accepted Xth XXXXXXXXX 20XX***
***First published on the web Xth XXXXXXXXXX 200X***
**DOI: 10.1039/b000000x**

Nanostructured, responsive hydrogels formed due to electrostatic interactions have promise for applications such as drug delivery and tissue mimics. These physically cross-linked hydrogels are composed of an aqueous solution of oppositely charged triblocks with charged end-blocks and neutral, hydrophilic mid-blocks. Due to their electrostatic interactions, the end-blocks microphase separate and form physical cross-links that are bridged by the mid-blocks. The structure of this system was determined using a new, efficient embedded fluctuation (EF) model in conjunction with self-consistent field theory. The calculations using the EF model were validated against unapproximated field-theoretic simulations with complex Langevin sampling and were found consistent with small angle X-ray scattering (SAXS) measurements on an experimental system. Using both the EF model and SAXS, phase diagrams were generated as a function of end-block fraction and polymer concentration. Several structures were observed including a body-centered cubic sphere phase, a hexagonally packed cylinder phase, and a lamellar phase. Finally, the EF model was used to explore how parameters that directly relate to polymer chemistry can be tuned to modify the resulting phase diagram, which is of practical interest for the development of new hydrogels.

## 1 Introduction

Composed of a three dimensional macroscopic network suspended in water, hydrogels are versatile and unique materials. The presence of a network introduces structural stability and allows one to tune functionality, while the high water content provides high compliance. Hydrogel networks, defined here as systems that exhibit a crossover in the shear loss and shear storage modulus, are typically composed of polymers that are either chemically cross-linked with covalent bonds or physically cross-linked through junctions that dynamically form, break and reform. Although gels formed using chemical cross-links often have superior mechanical properties, they are not as responsive to their environment and are not self-healing like their physically cross-linked counterparts. Consequently, much effort has been focused on the more versatile physically cross-linked hydrogels. Physical cross-links can be formed using a variety of methods including hydrogen bonding, hydrophobic interactions, electrostatic interactions and metal coordination [1,2] allowing them to respond to a wide array of environmental changes including temperature, pH, and ion concentration, among others. The resulting dynamic hydrogels are particularly useful for biomedical applications including drug delivery [3–6] and tissue growth scaffolds, [7–9] since the hydrogels can be designed to reproduce many of the properties of tissues while maintaining biocompatability. [10] Additionally, they can be used for bioadhesives and biosealants [11] and antifouling agents. [12,13]

One such class of dynamic hydrogels makes use of a phenomenon called complex coacervation, [14] which occurs when oppositely charged polyelectrolytes are mixed in aqueous solution. Due to the electrostatic attraction between the oppositely charged polymers, they aggregate and phase separate from water, forming a solvated, polymer rich, liquid phase known as a "complex coacervate." When the complementary polyelectrolytes are further elaborated into block copolymers, the coacervate phase can be nanostructured and either a liquid or soft solid. This technique has already been used extensively to study core-shell micelles produced by mixing diblock copolyectrolytes composed of one charged block and one neutral block with an oppositely charged homopolymer. [15–18]

Inspired by the work on core-shell micelles, in 2010, Lemmers *et al.* [19] reported the first coacervate inspired

† Electronic Supplementary Information (ESI) available: [details of any supplementary information available should be included here]. See DOI: 10.1039/b000000x/

[a] *Materials Research Laboratory, University of California, Santa Barbara, USA*
[b] *Department of Chemical Engineering, University of California, Santa Barbara, USA*
[c] *Materials Department, University of California, Santa Barbara, USA*
[d] *Department of Chemistry and Biochemistry, University of California, Santa Barbara, USA*
‡ Present address: National Institute of Standards and Technology
§ Present address: Illinois Applied Research Institute
¶ Present address: Lawrence Berkeley National Laboratory

hydrogels. Instead of using diblock copolyelectrolytes they used ABA triblock copolyelectrolytes of poly(3-sulfopropyl methacrylate)-poly(ethylene oxide)-poly(3-sulfopropyl methacrylate) (PSPMA-PEO-PSPMA) with negatively charged end-blocks (A) and a neutral, hydrophilic mid-block (B). For the homopolymer (C), they used poly(allylamine hydrochloride) (PAH), a polycation. At low concentrations of ABA triblock and homopolymer, flower-like micelles formed; however, when the concentration was increased, the neutral hydrophilic mid-blocks formed bridges between the coacervate domains, yielding a gel. Subsequently, Lemmers *et al.* created a phase diagram where both polymer concentration and salt concentration were varied,[20] calculated the fraction of mid-blocks that formed bridges,[20] and mixed different amounts of triblocks and homopolymers to investigate charge ratios, concluding that the optimal charge ratio was a stoichiometric mixture.[21]

Shortly after the initial study by Lemmers *et al.*,[19] Hunt *et al.*[22] reported mixing ABA triblocks with CBC triblocks instead of C homopolymer. They synthesized triblock copolyelectrolytes of poly(allyl glycidyl ether)-poly(ethylene oxide)-poly(allyl glycidyl ether) (PAGE-PEO-PAGE) and then functionalized the PAGE blocks with either sulfonate or carboxylate to form negatively charged triblocks (ABA) as well as with either guanidinium or ammonium to form positively charged triblocks (CBC). Significantly, formation of hydrogels could be tuned by the nature of the anion and cation with the most robust materials being obtained from the combination of sulfonate and guanidinium blocks. Additionally, with proper choices of polymer length and end-block fraction, they found that the coacervate domains formed spheres arranged on a body-centered cubic lattice unlike the gels created by Lemmers *et al.*,[19–21] which exhibited no long-range order. Using the system with sulfonate and guanidinium functionalized PAGE end groups, Krogstad *et al.*[23] generated a phase diagram where the polymer length and end-block fraction were fixed, while the total polymer concentration and added salt concentration were varied. In addition to body-centered cubic spheres, they also found hexagonally packed cylinders and regions of phase coexistence.

Developing theoretical models and computationally feasible simulation methods to study coacervation, and thus coacervate inspired hydrogels, is challenging. This challenge stems from the electrostatic nature of complex coacervation. Several theories that have been developed to describe coacervation in systems of homopolyelectrolytes[24–32] with varying degrees of approximations. Nonetheless, there is still no single established theory. An alternative approach has been to use computer simulations to study these systems.[33–44] However, most of these studies only considered a small number of homopolyelectrolytes such that phase behavior could not be determined. In order to determine the phase behavior of the homopolyelectrolyte system using simulations, field-theoretic simulations with complex Langevin sampling (FTS-CL)[45,46] can be used.[42–44] This technique samples the requisite electrostatic fluctuations around the saddle point and is able to predict coacervation unlike self-consistent field theory (SCFT), which invokes a mean-field approximation that cannot capture Debye-Hückel-like electrostatic correlation attractions.

Although other coacervate systems have been studied with theory and simulation,[47–51] coacervate inspired hydrogels have not been studied either theoretically or computationally to date. Here, we present the first computational study of coacervate inspired hydrogels and compare the results to experiments. In an effort to assist the development of new hydrogels, we investigated how the end-block fraction of the triblocks along with polymer concentration affected the self-assembled nanostructure of the resulting material. We compared computationally predicted structures with those determined by SAXS on a series of PAGE-based triblock coacervate gels.

In principle, FTS-CL can be used for simulation studies of complex coacervate gels, but we have found the cost of such simulations to be prohibitive given the broad range of possible morphologies and parameter spaces to be explored, and the lack of direct access to free energies. Instead, we developed a new embedded fluctuation (EF) model that can be used with SCFT, the latter technique being both computationally efficient and providing direct access to free energies. We demonstrate that the EF model is able to accurately and efficiently simulate hydrogel formation and structure by electrostatic complexation. This approach is different than that of Sing *et al.* who used a combination of SCFT and liquid state (LS) theory to simulate both unsolvated homopolyelectrolyte blends[52,53] and block copolyelectrolytes.[54] Specifically, they assumed that the system was homogeneous for length scales less than 1 nm, also known as a local homogeneity approximation, and used liquid state theory to predict a local chemical potential given the density. These local chemical potentials are then introduced into SCFT in order to calculate the density. The density is then used as an input for LS and the process is repeated until both SCFT and LS are self-consistent. Although this approach should work for complex coacervate gels, we opted to develop a new model that, despite being limited to parameter choices where ion binding is negligible, does not require a length scale choice above and below which interactions are treated in drastically different manners.

In the Methods section, we describe both the general polyelectrolyte model on which the new EF model is based and the EF model, itself. We also discuss the computational and experimental techniques used. In Results and Discussion, we present the phase diagram as predicted by the SCFT simulations of the EF model. Subsequently, we validate selected points on the phase diagram using full FTS-CL, as well as by directly comparing theoretical and experimental phase di-

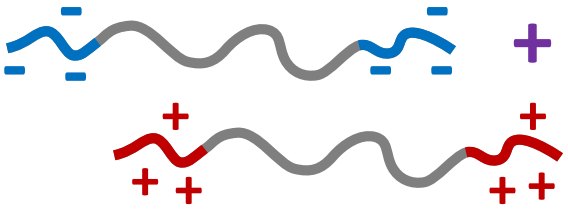

**Fig. 1** Diagram of the system with implicit solvent.

agrams as a function of both end-block fraction and polymer concentration and find good agreement. In addition to comparing the phase diagrams, we also compare domain spacings and present computational predictions for coacervate core size. Finally, we investigate how various choices of non-electrostatic segmental interactions, presumably tunable with polymer chemistry, can impact phase diagrams and coacervate hydrogel design using simulations with the EF model.

## 2 Models and Methods

### 2.1 Field-based model for use with complex Langevin simulations

The experimental system was modeled as a mixture of oppositely charged triblock copolyelectrolytes with charged end-blocks and neutral, hydrophilic mid-blocks dissolved in water as shown in Fig. 1. These $n$ polycations and $n$ polyanions with degree of polymerization of $N$ were taken to be symmetric with an end-block fraction of $f/2$ on each side. Additionally, the polycations and polyanions were identical except for the sign of the charge. For simplicity, the polyelectrolytes were assumed to be polyacids and polybases such that their counterions react to form water. The water is treated implicitly as a structureless dielectric continuum.

To describe the interactions between the triblock copolyelectrolytes, we adopted the model that Riggleman *et al.*[44] used to study mixtures of oppositely charged homopolyelectrolytes. The resulting particle-based canonical partition function is

$$\mathscr{Z}_C(2n,V,T) = \frac{1}{(n!)^2(\lambda_T^3)^{2nN}}\prod_{j=1}^{2n}\int \mathscr{D}\mathbf{r}_j \exp\left(-\sum_l \beta U_l[\mathbf{r}^{2nN}]\right) \quad (1)$$

where $U_l$ are the potential energy contributions, $\beta$ is $1/k_BT$, $\lambda_T$ is de Broglie wavelength, and the prefactor accounts for ideal contributions. There are three potential energy contributions: intramolecular interactions due to polymer connectivity, electrostatic interactions and non-ionic interactions. For simplicity, all lengths are scaled by the radius of gyration of the polymer $R_g$, which can be calculated via $\sqrt{Nb^2/6}$ where $b$ is the statistical segment length.

For the polymer connectivity, we used the continuous Gaussian chain model,[55] which results in

$$\beta U_0 = \frac{1}{4}\sum_{j=1}^{2n}\int_0^1 ds \left|\frac{d\mathbf{r}_j(s)}{ds}\right|^2 \quad (2)$$

where $s$ is a contour variable that varies from 0 at one end of the chain to 1 at the other end of the chain, and $\mathbf{r}_j(s)$ represents the vector that points to position $s$ along chain $j$. The electrostatic interactions are described by a Coulomb potential:

$$\beta U_{el} = \frac{\ell_B N^2\sigma^2}{2}\int d\mathbf{r}\int d\mathbf{r}'\,(\hat{\rho}_{e+}(\mathbf{r})-\hat{\rho}_{e-}(\mathbf{r}))\frac{1}{|\mathbf{r}-\mathbf{r}'|}\left(\hat{\rho}_{e+}(\mathbf{r}')-\hat{\rho}_{e-}(\mathbf{r}')\right) \quad (3)$$

where $\ell_B$ is the Bjerrum length, $\sigma$ is the fraction of monomers on the charged blocks bearing charge (assumed the same for anionic and cationic blocks), and $\hat{\rho}_{e+}$ and $\hat{\rho}_{e-}$ are the total microscopic densities for the positively and negatively charged end-blocks, respectively. The Bjerrum length ($\ell_B \equiv e^2k_BT/\varepsilon$) represents the length scale at which the energy to separate two unit charged ions in the solvent medium is equivalent to the thermal energy $k_BT$. $\varepsilon$ is the dielectric constant of the solvent, in this case water, and $e$ is the charge of an electron. In writing Eq. 3, the dielectric constant is assumed to be spatially invariant and equal to that of water, so that the Bjerrum length is roughly 0.7 nm.

The microscopic density for a polymer block $\hat{\rho}_b$ is

$$\hat{\rho}_b(\mathbf{r}) = \sum_{j=1}^{n}\Gamma(\mathbf{r}) * \int_\alpha^\xi ds\,\delta(\mathbf{r}-\mathbf{r}_j(s)). \quad (4)$$

$\alpha$ and $\xi$ refer to the value of $s$ at the start and end of the block, respectively, and $*$ represents a convolution. $\Gamma$ is a smearing function chosen to be a normalized Gaussian

$$\Gamma(\mathbf{r}) = \left(\frac{1}{2\pi a^2}\right)^{3/2}\exp(-|\mathbf{r}|^2/(2a^2)) \quad (5)$$

where $a$ is a smearing parameter, which we have taken to be 0.15 $R_g$. The introduction of this smearing is a regularization technique that eliminates UV divergences for both electrostatic and non-ionic interactions in the field-based model when using FTS-CL (see work by Riggleman *et al.* for a more complete discussion[44] and original treatment of ions by Wang[56]). Since our model is already a coarse-grained representation of the system, the introduction of smearing, an inherently coarse-grained approach, should not affect the predicted trends in morphology.

The non-ionic interactions were modeled via an extension the Edwards model[57] of contact interactions[55,58] such that water is treated implicitly. This potential energy is

$$\beta U_{exv} = \frac{1}{2}\int d\mathbf{r}\, P(\mathbf{r})^T \mathbf{B} P(\mathbf{r}) \tag{6}$$

where

$$\mathbf{B} = \begin{pmatrix} B_{ee} & B_{em} \\ B_{em} & B_{mm} \end{pmatrix}, \tag{7}$$

$$P(\mathbf{r}) = \begin{pmatrix} \hat{\rho}_{e+}(\mathbf{r}) + \hat{\rho}_{e-}(\mathbf{r}) \\ \hat{\rho}_{m+}(\mathbf{r}) + \hat{\rho}_{m-}(\mathbf{r}) \end{pmatrix}. \tag{8}$$

$B_{jl}$ is the excluded volume parameter between species $j$ and species $l$ multiplied by $N^2$ and made dimensionless by dividing by a factor of $R_g^3$. The additional densities, $\hat{\rho}_{m+}$ and $\hat{\rho}_{m-}$ are the densities for mid-blocks on the positively and negatively charged polyelectrolytes, respectively.

Given the canonical partition function, we used Hubbard-Stratonovich transformations[59] to convert the particle-based model to a mathematically equivalent field-based model. Prior to implementation of the transformation, the excluded volume interactions were first decoupled using a Eigen decomposition of the $B_{ij}$ matrix resulting in eigenvalues $d_j$ and eigenvectors $\begin{pmatrix} U_{1j} & U_{2j} \end{pmatrix}$. A detailed discussion of the Eigen decomposition can be found in the SI. The application of the transformations yields the canonical partition function

$$\mathscr{Z}_C(2n,V,T) = \mathscr{Z}_0 \int \mathscr{D}w_1 \int \mathscr{D}w_2 \int \mathscr{D}\psi \exp(-H[w_1,w_2,\psi]) \tag{9}$$

where $w_j$ is a chemical potential field conjugate to $(U_{1j}(\hat{\rho}_{e+} + \hat{\rho}_{e-}) + U_{2j}(\hat{\rho}_{m+} + \hat{\rho}_{m-}))$, $\psi$ is an electrostatic potential field, and $\mathscr{Z}_0$ includes ideal and normalization terms. Of the terms in $\mathscr{Z}_0$, the only contributions necessary for simulating the system are the ideal terms, which are $(V^n/n!)^2$; the remainder of the terms in $\mathscr{Z}_0$ are linear in $n$ resulting in constant shifts in the chemical potentials leaving phase behavior unaffected. The Hamiltonian $H$ is written

$$H[w_1,w_2,\psi] = \sum_{j=1}^{2} \frac{1}{2|d_j|}\int d\mathbf{r}\, w_j(\mathbf{r})^2 - n\ln Q[w_+ * \Gamma] - \frac{1}{2E}\int d\mathbf{r}\, \psi(\mathbf{r})\nabla^2\psi(\mathbf{r}) - n\ln Q[w_- * \Gamma] \tag{10}$$

where

$$w_+ = \begin{cases} \sum_{j=1}^{2} U_{2j}\xi_j w_j & f/2 < s < 1-f/2 \\ \sum_{j=1}^{2} U_{1j}\xi_j w_j + i\psi & \text{otherwise} \end{cases}, \tag{11}$$

$$w_- = \begin{cases} \sum_{j=1}^{2} U_{2j}\xi_j w_j & f/2 < s < 1-f/2 \\ \sum_{j=1}^{2} U_{1j}\xi_j w_j - i\psi & \text{otherwise} \end{cases}, \tag{12}$$

$$\xi_j = \begin{cases} i & d_j > 0 \\ 1 & d_j < 0 \end{cases}, \tag{13}$$

and $E = 4\pi\ell_B N^2\sigma^2 R_g^{-1}$. $i$ is unit imaginary number.

The single chain partition function $Q$ can be computed from

$$Q[w_\pm * \Gamma] = \frac{1}{V}\int d\mathbf{r}\, q(\mathbf{r},1;[w_\pm * \Gamma]) \tag{14}$$

where $q(\mathbf{r},s;[w_\pm * \Gamma])$ is calculated from

$$\frac{\partial}{\partial s} q(\mathbf{r},s;[w_\pm * \Gamma]) = \nabla^2 q(\mathbf{r},s;[w_\pm * \Gamma]) - (w_\pm(\mathbf{r},s) * \Gamma(\mathbf{r}))\, q(\mathbf{r},s;[w_\pm * \Gamma]) \tag{15}$$

subject to the initial condition $q(\mathbf{r},s=0;[w_\pm * \Gamma]) = 1$. In addition to being used to calculate $Q$, $q$ is also used to calculate the density *operator* $\tilde{\rho}(\mathbf{r})$ such that $\langle\hat{\rho}(\mathbf{r})\rangle = \langle\tilde{\rho}(\mathbf{r})\rangle$ where the brackets represent ensemble averages and the introduction of $\Gamma$ is factored out so that the density operators have their traditional definition. Thus, the density operators for the mid-blocks and end-blocks can be expressed as

$$\tilde{\rho}_{m\pm}(\mathbf{r}) = \frac{C}{2Q_\pm}\Gamma(\mathbf{r}) * \left(\int_{f/2}^{1-f/2} ds\, q(\mathbf{r},1-s;[w_\pm * \Gamma])\, q(\mathbf{r},s;[w_\pm * \Gamma])\right), \tag{16}$$

$$\tilde{\rho}_{e\pm}(\mathbf{r}) = \frac{C}{2Q_\pm}\Gamma(\mathbf{r}) * \left(\int_0^{f/2} ds\, q(\mathbf{r},1-s;[w_\pm * \Gamma])\, q(\mathbf{r},s;[w_\pm * \Gamma]) + \int_{1-f/2}^{1} ds\, q(\mathbf{r},1-s;[w_\pm * \Gamma])\, q(\mathbf{r},s;[w_\pm * \Gamma])\right) \tag{17}$$

where $C = 2nR_g^3/V$ is the concentration.

### 2.2 Motivation for the development of the embedded fluctuation model

If the general model described in Sec. 2.1 was used with the most common field-based simulation technique, SCFT,[59–61] the model would only predict a single perfectly homogeneous phase rather than the expected microphase separation.[42,43] This prediction is due to the saddle point approximation, which assumes that a single configuration dominates the functional integrals. For coacervate systems with the type of model described in Sec. 2.3, this assumption is erroneous and at least Gaussian-level fluctuations in the electrostatic potential field $\psi$ must be retained to generate the net electrostatic attraction required for coacervation. Instead, the model can be used with

FTS-CL, which unlike SCFT does not invoke any approximations. This technique, developed by Fredrickson and Ganesan,[45,46] samples the statistics of the full field-based canonical partition function.

However, generating a phase diagram for our system using FTS-CL would have been a formidable task given the current state of development. Although methods exist for computing the free energy[62] and simulating phase coexistence,[63] they are both computationally demanding and have not previously been used in tandem. Additionally, no technique has been established to determine the domain spacing in unit cell calculations for FTS-CL. In contrast, for SCFT, the free energy is directly accessible and determining both phase coexistence[64] and the optimal domain spacing[65] is straightforward. Thus, we developed a new EF model that can accurately predict the phase behavior of a triblock copolyelectrolyte system when simulated with SCFT.

### 2.3 New embedded fluctuation (EF) model for use with SCFT

Since the *electrostatic* interactions are the driving force for the observed phase behavior,[42,43] we only need to embed the electrostatic fluctuations. To do this, we make use of an analytic technique called the one-loop approximation,[26–31,47] which has previously been shown to qualitatively mimic the phase behavior for mixtures of oppositely charged homopolyelectrolytes.[42–44] This technique involves expanding the Hamiltonian to second order in the fields around the homogeneous saddle point and then evaluating the Gaussian functional integrals such that the free energy is explicitly computed. Following this procedure, we find that the electrostatic contribution to the free energy is

$$\beta F_{el}^{one-loop} = \frac{V}{4\pi^2}\int_0^\infty dk\, k^2 \ln\left(1+(Cf)\frac{E\hat{g}_{D,e}(f,k^2)\hat{\Gamma}^2(k^2)}{fk^2}\right) \quad (18)$$

where

$$\hat{g}_{D,e}(f,k^2) = \frac{2}{k^4}(-2+fk^2+2e^{-(f/2)k^2} + e^{(f-1)k^2} - 2e^{(f/2-1)k^2} + e^{-k^2}) \quad (19)$$

is a Debye-like function. Since we are interested in microphase separation rather than the macrophase separation of earlier studies, we seek a local effective electrostatic potential with the same integrated strength in a homogeneous system. Noticing that $Cf$ is the homogeneous expression for the total end-block density, we replace Eq. 3 with the following "effective" electrostatic potential energy.

$$\beta U_{el} = \frac{1}{4\pi^2}\int d\mathbf{r}\int_0^\infty dk\, k^2 \ln\left(1+(\hat{\rho}_{e+}(\mathbf{r})+\hat{\rho}_{e-}(\mathbf{r}))\frac{E\hat{g}_{D,e}(f,k^2)\hat{\Gamma}^2(k^2)}{fk^2}\right) \quad (20)$$

Note that the factor of $V$ in the free energy was replaced by an integral over space and that the relevant density is the *total* end-block density rather than the charge density as in Eq. 3. This is not surprising since we would expect the positions of the positively and negatively charged end-blocks to be highly correlated given the nature of the phase separation. Our effective electrostatic potential now has local dependence and second order electrostatic fluctuations embedded at zeroth order such that SCFT can be used with the model once it is in a field-based framework.

To develop the new field-based framework, we made use of Hubbard-Stratonovich transformations with explicit density fields. These explicit density fields, $\rho_e$ and $\rho_m$, are defined to be equal to $(\hat{\rho}_{e+}(\mathbf{r})+\hat{\rho}_{e-}(\mathbf{r}))$ and $(\hat{\rho}_{m+}(\mathbf{r})+\hat{\rho}_{m-}(\mathbf{r}))$, respectively. Thus, the EF model is a psuedo one component system, since the polycation and polyanion are no longer required to be treated separately. The new canonical partition function is

$$\mathscr{Z}_C(2n,V,T) = \mathscr{Z}_0\int\mathscr{D}\rho_e\int\mathscr{D}\rho_m\int\mathscr{D}w\int\mathscr{D}\psi \exp(-H[\rho_e,\rho_m,w,\psi]) \quad (21)$$

where $\mathscr{Z}_0$ accounts the ideal terms and normalization terms but is different than the $\mathscr{Z}_0$ in Eq. 9. The new Hamiltonian is

$$H[w,\psi,\rho_m,\rho_e] = \frac{1}{4\pi^2}\int d\mathbf{r}\int_0^\infty dk\, k^2 \ln\left(1+\rho_e\frac{E\hat{g}_{D,e}(f,k^2)\hat{\Gamma}^2(k^2)}{fk^2}\right) + \frac{1}{2}\int d\mathbf{r}\begin{pmatrix}\rho_m(\mathbf{r})\\ \rho_e(\mathbf{r})\end{pmatrix}^T\begin{pmatrix}B_{mm} & B_{em}\\ B_{em} & B_{ee}\end{pmatrix}\begin{pmatrix}\rho_m(\mathbf{r})\\ \rho_e(\mathbf{r})\end{pmatrix} - \int d\mathbf{r}\, iw(\mathbf{r})\rho_m(\mathbf{r}) - \int d\mathbf{r}\, i\psi(\mathbf{r})\rho_e(\mathbf{r}) - CV\ln Q[\Gamma * w'] \quad (22)$$

where

$$w' = \begin{cases} iw & f/2 < t < 1-f/2 \\ i\psi & \text{otherwise}\end{cases}. \quad (23)$$

The first two terms in the Hamiltonian represent the electrostatic (Eq. 20) and excluded volume (Eq. 6) interactions, respectively. The next two terms are effectively Lagrange multipliers to ensure that the density fields match the microscopic densities, and the final term accounts for the polymer connectivity.

The electrostatic contribution to the Hamiltonian requires the evaluation of a numerical integral in the inner loop of the SCFT simulations. Since we wanted to avoid this computationally expensive step, we made use of a fitting function and additional simplifications; the details can be found in the SI.

### 2.4 Numerical methods

For our SCFT simulations of the EF model (see Sec. 2.3), we first simplified the forces, the details of which can be found in the SI. We then used a steepest descent scheme with Euler updates requiring the $\ell^2$ norm of the forces to be less than $10^{-6}$. A fourth-order method proposed by Ranjan, Qin and Morse[66] with a contour resolution of $\Delta s = 1/200$ was used to solve the modified diffusion equation and a spatial grid with $\Delta x \leq 0.2R_g$ was adopted. In order to find the proper domain spacing, we used a variable cell technique[65] and required that the $\ell^2$ norm of the derivative of the intensive free energy with respect to the shape tensor was less than $10^{-4}$. Additionally, to compute regions of phase coexistence we made use of the Gibbs ensemble[67,68] that has recently extended to field-based models.[63,64] We use an adaptation of the method described by Mester *et al.*;[64] our variant used the pseudo-spectral rather than spectral method along with steepest descent. We required that the $\ell^2$-norm of each of the forces on concentrations and volume fractions were less than $10^{-6}$. We found that these choices were sufficient to determine phase boundaries within the thickness of the indicated phase boundary lines.

FTS-CL simulations of the general polyelectrolyte model (see Sec. 2.1) were used to validate the phase diagrams generated with the EF model. For simulations of microphases with long-range order, we used three dimensional versions of the primitive cells. The simulation cell sizes were chosen to correspond to stress-free configurations determined from SCFT simulations of the EF model. We found that FTS-CL simulations initialized with random values for the fields produced defective phases. However, when the simulation cell size was adjusted slightly, the expected ordered phases emerged. Using the fields from these simulations as seeds, we reran simulations with the SCFT stress-free simulation cell shapes, replicated the unit cell in each dimension, reequilibrated the simulation and computed the structure factor for the end-block/end-block density (see SI for derivation). All FTS-CL simulations were run using a second-order method[69,70] for the pseudo-spectral chain propagator solutions with $\Delta s = 1/100$. A predictor-corrector variant of Euler-Maruyama[71] was used for the pseudo-time integration with $\Delta t = 0.5$ for systems with long-range order, and either $\Delta t = 0.05$ or $0.025$ for systems without long-range order. We also required spatial resolution of $\Delta x \leq 0.2R_g$.

### 2.5 Experimental methods

The triblock copolymers were synthesized by anionic ring open polymerization of allyl glycidyl ether from a PEO-diol macroinitiator and functionalized with sulfonate or guanidinium using thiol-ene click chemistry as described previously by Hunt *et al.*[22] A series of triblock copolymers were made with varying end-block length and a mid-block with a number-average molecular weight of 10,000 Da. The end-blocks length ranged from 15 to 50 repeat units on each end as determined by $^1$H NMR. The polydispersity for each polymer ranged between 1.08 and 1.12 as determined by size exclusion chromatography relative to polystyrene standards.

Hydrogels were prepared in two different ways. Solutions of less than 35 wt% were generated by dissolving the functionalized polymers separately in water at a stoichiometric ratio and the desired concentration. The sulfonate-functionalized polymer solution was then added to the guanidinium-functionalized polymer solution and mixed with a vortex mixer for 30 seconds. Solutions of 35 wt% or greater were generated by first mixing the dry functionalized polymers and then adding the desired amount of water. The gels were then allowed to rest for at least 12 hours before they were loaded into 1.5 mm diameter quartz capillaries to be used for small angle X-ray scattering (SAXS). SAXS experiments were carried out at the Stanford Synchrotron Radiation Lightsource using 7.1 keV X-rays and a detector distance of 2.1 meters as well as the Advanced Photon Source, Argonne National Laboratory with beamline 8-ID-E using 7.35keV X-rays and a detector distance of 2.18m.

$^1$H NMR spectroscopy was carried out on a Bruker AC 500 spectrometer in deuterated chloroform. Size exclusion chromatography was performed on a Waters Alliance HPLC System 2690 Separation Module chromatograph with two Agilent PLGEL 5$\mu$m, MIXED-D, 300x7.5 mm columns for fractionation. A Waters 2414 differential refractometer and a 2996 photodiode array detector were used for detection of eluent. Chloroform with 0.1% tetraethylamine at room temperature was used as the mobile phase. Calibration was carried out against polystyrene and poly(ethylene oxide) standards.

## 3 Results and Discussion

### 3.1 Phase diagram for the embedded fluctuation model

Using our model with embedded fluctuations, we generated a theoretical phase diagram as a function of end-block fraction and polymer concentration. The electrostatic strength parameter $E$ was a set a value of 500,000, and the non-electrostatic excluded volume parameters were set to $B_{ee} = 1$ and $B_{em} = B_{mm} = 3$, i.e. a situation where the potential of mean force is more strongly repulsive for end-middle or middle-middle pairs

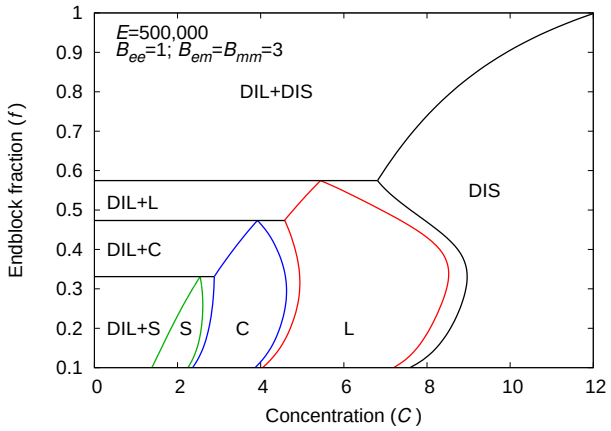


**Fig. 2** Phase diagram for $E = 500,000$, $B_{ee} = 1$ and $B_{em} = B_{mm} = 3$ using the EF model. Observed phases included disordered (DIS), dilute (DIL), either body-centered cubic spheres or face-centered cubic spheres (S), hexagonally packed cylinders (C), lamellae (L) and regions of phase coexistence.

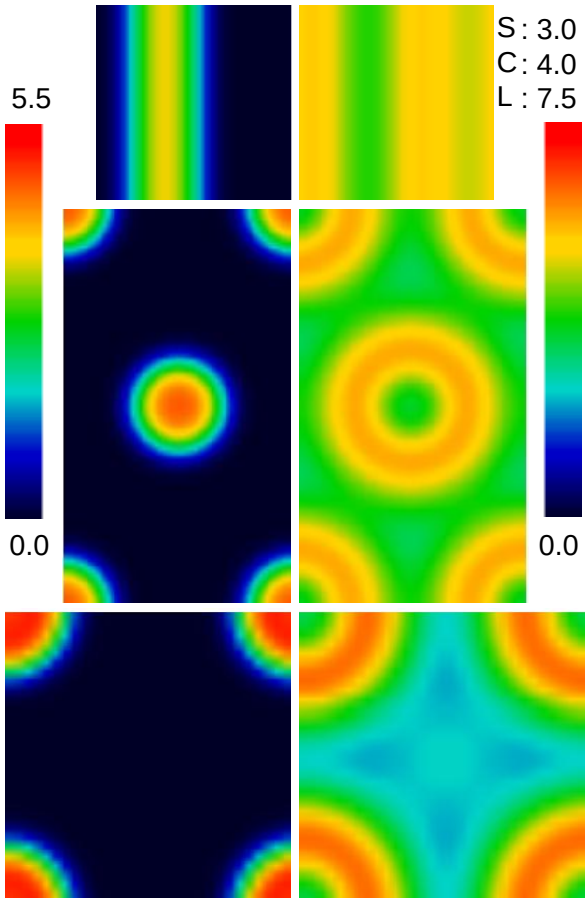


**Fig. 3** Cross-sections of end-block (left) and mid-block (right) densities of, from top to bottom, lamellae at $C = 6$, hexagonally packed cylinders at $C = 3$, and body-centered cubic spheres at $C = 2$. Parameters are $f = 0.2$, $E = 500,000$, $B_{ee} = 1$ and $B_{em} = B_{mm} = 3$. The mid-block scale bar depends on the structure with L corresponding to lamellae ($C = 6$), C corresponding to hexagonally packed cylinders ($C = 3$) and S corresponding to body-centered cubic spheres ($C = 2$).

of polymer segments than for end-end segmental interactions. This phase diagram, as can be seen in Fig. 2, contained several different phases including a polymer rich homogeneous phase denoted as DIS, a nearly pure water phase denoted as DIL for dilute, lamellae denoted as L, hexagonally packed cylinders denoted as C and a spherical phase denoted as S. For the spherical phase, we were unable to distinguish body-centered cubic spheres and face-centered cubic due to the small difference in their free energies. In addition to several single phase regions, the phase diagram also has several regions of phase coexistence including phase coexistence between two microphases and phase coexistence between a microphase and pure water. As expected, microphases were stable at lower end-block fractions, while macrophase separation is stable at high end-block fractions. At low end-block fractions ($f \leq 0.32$), the concentration could be tuned to select the desired microphase, which is of practical interest since these systems could be either hydrated or dehydrated in order to change their morphology.

In order to characterize the structures of the microphases, we plotted cross-sections of both the end-block and mid-block densities at $f = 0.2$ and various concentrations ($C$) in Fig. 3. Note that the concentration unit is a measure of the number of polymers per volume scaled by the cubed radius of gyration; thus, it scales as the degree of polymerization to the $3/2$ power. We found that for all of the concentrations, the end-block density was concentrated in the coacervate domains leaving essentially zero end-block density in the interstitial sites such that the coacervate domains formed well defined physical cross-link junctions. Comparing the end-block and mid-block densities, we found that the mid-block density reached a maximum at the coacervate interface, which was likely due to a balance between the dislike of the end-blocks and mid-blocks characterized by $B_{em}$, their chemical connectivity which prohibits macrophase separation, and their solvation. In the interstitial sites, the mid-block density was slightly lower than the maximum but was still significantly higher than that of the end-block.

Another interesting feature is that the maximum end-block density was only slightly dependent on the total concentration at fixed end-block fraction. This can be seen by comparing the cross-sections of the end-block fractions in Fig. 3; this was in contrast to the maximum mid-block density, which was highly dependent on the total polymer concentration. However, when the end-block fraction was adjusted and the total concentration was fixed, both the maximum end-block and mid-block densi-

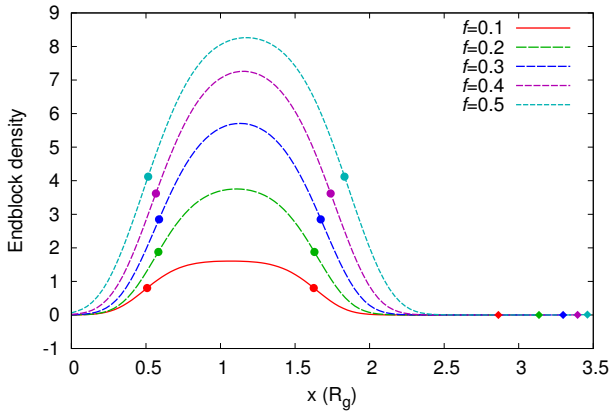


**Fig. 4** End-block density profiles for the lamellar phase at $C = 6$ and various end-block fractions for a unit cell. Other parameters are $E = 500,000$, $B_{ee} = 1$ and $B_{em} = B_{mm} = 3$. The circles denote the half-max concentration, which is discussed in Sec. 3.3 while the diamonds represent the end of the unit cell.

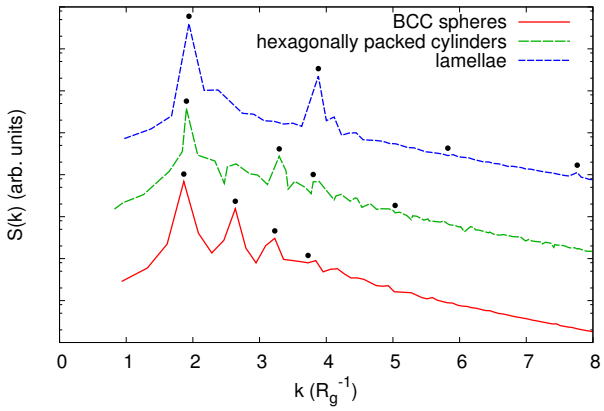


**Fig. 5** End-block/end-block structure factors of body-centered cubic spheres at $C = 2$, hexagonally packed cylinders at $C = 3$, and lamellae at $C = 6$. Other parameters are $f = 0.2$, $E = 500,000$, $B_{ee} = 1$ and $B_{em} = B_{mm} = 3$. Data were generated using the general model and FTS-CL.

ties were highly dependent on the end-block fraction as seen in Fig. 4 where the end-block density was plotted for various end-block fractions with $C = 6$.

### 3.2 Validation of the embedded fluctuation model using complex Langevin simulations

To validate the EF model, we reproduced various points on the phase diagram in Fig. 2 by using FTS-CL simulations of the general polyelectrolyte model (see Eqs. 9 and 10). For the microphases, we ran simulations and computed the end-block/end-block structure factor (see SI for derivation) for the same points as in Fig. 3, which occur at $f = 0.2$ and $C = 2, 3$ and 4 corresponding to body-centered cubic spheres, hexagonally packed cylinders and lamellae, respectively. The resulting structure factors are shown in Fig. 5 where the dots correspond to the expected peak locations based on the expected structure and primary peak. Clearly, each resulting simulation yielded the expected morphology. Additionally, if we compared the density profiles from the model with embedded fluctuations (see Fig. 3) with the averaged density cross-sections from the unit-cell simulations (see SI), the maximum and minimum densities are similar. Ultimately, these results suggested that the phases predicted with the new model are at least metastable using the original model. This agreement was better than expected considering that the new model only embeds electrostatic fluctuations up to second order, while the full FTS-CL include electrostatic fluctuations to *all* orders.

### 3.3 Validation of embedded fluctuation model with experimental phase diagram

An experimental phase diagram for the triblock system is shown in Fig. 6. In order to explicitly compare these experimental results with the theoretical phase diagram in Fig. 2, we computed the experimental end-block fractions. This was done by using the number of monomers computed from the molecular weights for both the end-blocks and the mid-blocks. For the polymer concentration, rather than converting from weight percent polymer to the $C$ parameter, which is implicitly dependent on molecular weight, we chose to use the experimental units for experimental data. However, in order to make an appropriate comparison, the concentration for the theoretical phase diagram in the inset of Fig. 6 was adjusted so that rather than having a fixed molecular weight, the molecular weight increases with end-block fraction as in the experimental phase diagram (see experimental methods for details). We note that quantitative agreement is not possible due to uncertainties associated with mapping experimental parameters to theoretical parameters. Specifically, $R_g$ represents the unperturbed radius of gyration, which is difficult to determine experimentally. Since $R_g$ scales all relevant parameters ($C$, $E$, $B_{ij}$) accurate determination of its value is critical. Also, since the molecular weight varies in the experimental system, it means that the relevant parameters will also vary. Thus, we focus on the determination of trends, which should be accurate.

Experimentally, several phases were observed including body-centered cubic spheres denoted as S, hexagonally packed cylinder denoted as C, bicontinuous gyroid denoted

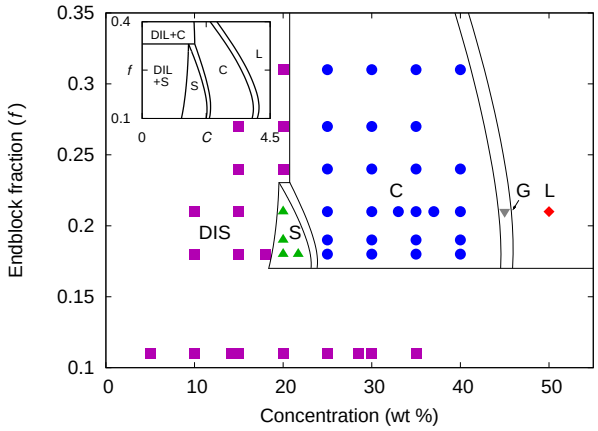


**Fig. 6** Experimental phase diagram. Observed phases include disordered (DIS), body-centered cubic spheres (S), hexagonally packed cylinders (C), bicontinuous gyroid (G), and lamellae (L). Disordered phases correspond to any SAXS pattern where higher order peaks were not observed. Lines are provided for guidance only and mimic the EF model phase diagram. The inset shows the relevant theoretical phase diagram with the concentration units adjusted such that the polymer length increases with end-block fraction as in the experimental system.

as G, lamellae denoted as L and a disordered phase denoted as DIS. The structure of each sample was determined by identifying peak positions in SAXS experiments. As an example, the SAXS results for $f = 0.21$ can be found in the SI. For the disordered phase, no well defined secondary peak was observed.

The experimental and theoretical phase diagrams were found to be qualitatively similar despite the fact that the relevant theoretical parameters ($B_{ij}$, $E$) do not exactly match the experimental system. For example, the same microphases—spheres, hexagonally packed cylinders, and lamellae—were observed with increasing concentration with the exception of the experimental gyroid phase, which might be metastable as predicted theoretically, since hydrogels with high concentrations, such as 45 wt %, are more likely to be trapped in a metastable state due to the slow kinetics of forming gels with high concentrations. Also at such high concentrations, it is difficult to create the samples due to the polymer solubility, which is likely why only a single lamellar sample was observed. Although phase coexistence is not observed for the experimental data points, it is possible that phase coexistence could be present in the experimental system. Previous work by Krogstad *et al.*[23] with a very similar experimental system found coexistence of microphases. In addition to the same order of observed microphases, the experimental body centered cubic sphere phase also pinches off at higher end-block fraction just as in the theoretical phase diagram.

The only other qualitative difference between the experimental and theoretical results was the presence of a disordered phase both at low end-block fraction and concentration experimentally. For the low concentration, theoretically only systems with long-range order were considered and thus it was not possible to predict microphase separation without long-range order, a result consistent with the experimental SAXS measurements. However, the regions of the disordered phase experimentally correspond roughly to microphase/dilute phase coexistence. As for very low end-block fraction, theoretically, one would expect a uniform disordered phase without microphase separation since the electrostatics would no longer be able to drive coacervation and thus hydrogel formation. The difference at low end-block fraction suggests that the parameter choices for the theoretical model probably do not align with the parameters for the experimental system. Despite these minor differences, the theoretical and experimental phase diagrams are qualitatively similar.

We next compared changes in the domain spacing of the microphase-separated structures as a function of polymer concentration. The domain spacings were defined as $2\pi/k^*$ where $k^*$ is the wavevector of the primary peak of either the calculated structure factor or the experimental scattering data. The resulting domain spacings can be found in Fig. 7. For the experimental domain spacings, each point in Fig. 7a corresponded to a point on the phase diagram (see Fig. 6), and for the theoretical domain spacing, gaps in the domain spacing data corresponded to regions of phase coexistence on the phase diagram. In general, we found that both the experimental and theoretical domain spacings have qualitatively similar trends. The domain spacing decreased with increasing concentration for a fixed phase, which was likely due to reduced swelling of the mid-block domains by water. Also, the domain spacing increased with increasing end-block fraction as expected. Theoretically, large jumps in the domain spacing were predicted between the hexagonally packed cylinder phase and the lamellar phase, while experimentally, it was not clear if such jumps exist due to the single lamellar point. If we use a back of the envelope calculation to estimate $R_g$ based on the number of repeat units and the statistical segment length of PEO, we find that the theoretical domain spacings vary from 15 to 26 nm, in line with experimental results.

We also determined the theoretical coacervate core diameter or width. Using the half-max of the end-block concentration to define the size of the coacervate core, we computed the diameter of the spheres for body-centered cubic spheres, the diameter of the cylinders for hexagonally packed cylinders, and the width of the coacervate domain for lamellae. Computing such quantities experimentally would be challenging and normally requires performing multi-parameter fits on SANS data or the use of cryo-TEM.[72] Thus, we expect our predictions will be of practical use in interpreting experimental data, formulating and validating new fitting models for small angle

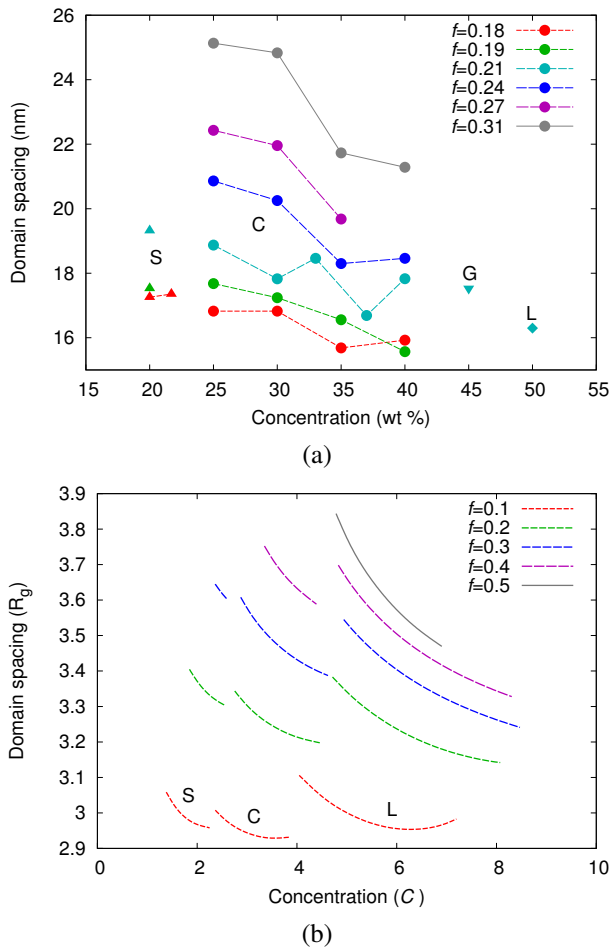


**Fig. 7** (a) Experimental domain spacings and (b) the corresponding theoretical domain spacings with $E = 500,000$, $B_{ee} = 1$ and $B_{em} = B_{mm} = 3$. Symbols in (a) correspond to different phases.

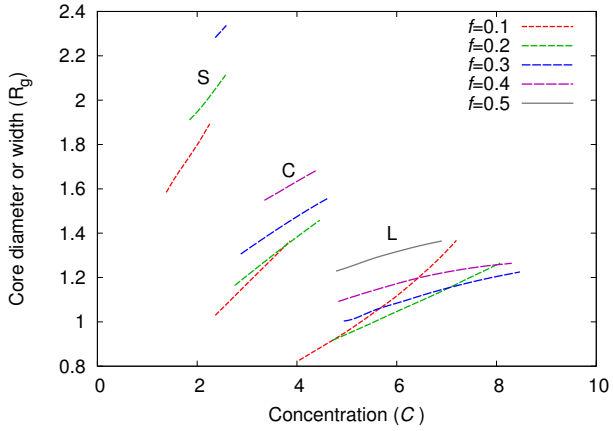


**Fig. 8** Theoretical coacervate core sizes for various end-block fractions.

scattering data.

The resulting theoretical coacervate core sizes are plotted in Fig. 8. We found that the diameter for body-centered cubic spheres was normally larger than the cylinder diameter for hexagonally packed cylinders. This result is not surprising since for the same volume of coacervate, the diameter for spheres would be larger than that of cylinders. Similarly, the cylinder diameter for hexagonally packed cylinders was normally larger than the lamellae width. In general, we also found that the core size increased with increasing end-block fraction. The non-monotonic changes for lamellae is merely an artifact of using the half-max concentration to define the core size. This can be seen in Fig. 4.

In conclusion, we have found that the general trends from the theoretical phase diagram generally correspond to experimental observations. Additionally, we found similar agreement for the domain spacing. We also have computed coacervate core size, which is difficult to probe experimentally.

### 3.4 Controlling hydrogel structure by adjusting interactions

The EF model represents a useful tool to predict the role of polymer interactions on mesostructure by generating theoretical phase diagrams for different nonbonded segmental interaction parameters and electrostatic strengths. Given the qualitative agreement between the experimental and theoretical phase diagrams, we expect these results will provide guidance for future experimental studies. This allows us to predict trends without directly mapping experimental quantities to theoretical parameters, which can be quite challenging. In particular, we determined how the phase boundaries shift as both $B_{em}$ and $B_{mm}$ increase, $B_{ee}$ decreases, and $E$ decreases. The corresponding phase diagrams are in Fig. 9, which should be directly compared to Fig. 2.

First, we considered increasing $B_{em}$ and $B_{mm}$. $B_{em}$ corresponds to the dislike of the mid-blocks and the end-blocks; thus, it could be qualitatively thought of as a solvent mediated $\chi$ parameter. Conversely, $B_{mm}$ is a measure of solvent quality for the middle blocks such that higher values correspond to a more hydrophilic polymer. Therefore, increasing $B_{em}$ and $B_{mm}$ could be experimentally realized by using a more hydrophilic mid-block that has a larger $\chi$ parameter with the end-block. Comparing Fig. 2 with Fig. 9a, we found that increasing both $B_{em}$ and $B_{mm}$ significantly expands the size of the microphase separation regions to both higher and lower concentration as well as to higher end-block fraction. This effect is apparently dominated by the larger value of $B_{em}$, which, like a $\chi$ parameter, promotes microphase separation even in the absence of electrostatics. Confirming this idea, we found two different lamellar phases at high concentrations ($C \geq 9.5$). The first has an end-block density profile similar to those at lower concen-

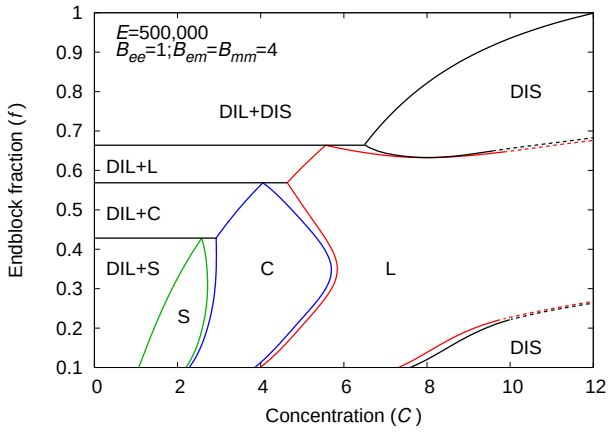


(a)

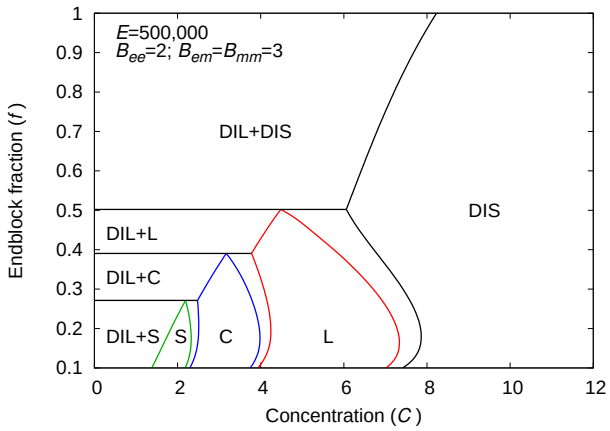


(b)

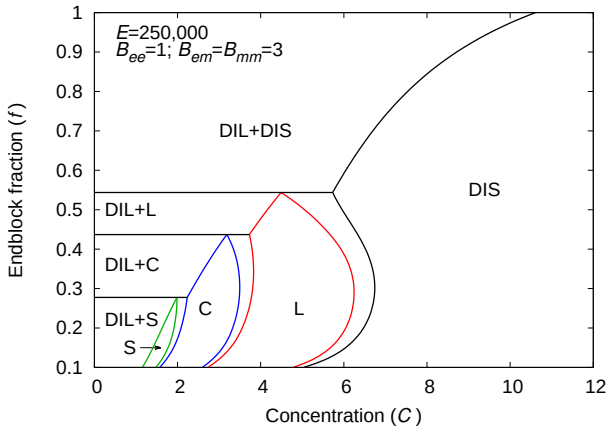


(c)

**Fig. 9** Phase diagram for various parameters using the EF model. Observed phases included disordered (DIS), dilute (DIL), either body-centered cubic spheres or face-centered cubic spheres (S), hexagonally packed cylinders (C), lamellae (L) and regions of phase coexistence. Dashed lines are described in the text.

tration, while the other does not have end-block densities that approach zero. Since the concentrations required to see observed different types of lamellae are high enough that they are not relevant for hydrogel applications, we have used dashed lines to denote estimated phase boundaries between the lamellar and homogeneous phases. Such an estimate was required due to small differences in the phase boundaries if only one of the two lamellar phases was considered.

Second, we increased the value of $B_{ee}$, which is a measure of the end-block solubility with larger values corresponding to a more hydrophilic end-block. Since improved end-block solvent quality competes with electrostatic attractions to inhibit coacervation, we found smaller microphase regions for $B_{ee} = 2$ (see Fig. 9b) than for $B_{ee} = 1$ (see Fig. 2). However, the effect was relatively small, only shifting the microphase/macrophase boundary from $f = 0.5$ for $B_{ee} = 2$ to $f = 0.57$ for $B_{ee} = 1$ despite the doubling of the parameter. This suggests that if the electrostatics are strong enough, the hydrophilicity of the end-block may only play a minor role.

Finally, we investigate the role of $E$, which is a measure of the electrostatic strength. Experimentally, this could be accomplished by reducing the charge density on the end-blocks (note $E$ is proportional to $\sigma^2$). Since the coacervate hydrogels were formed due to electrostatic interactions, a decrease in $E$ decreases the driving force for microphase separation. However, since the electrostatic interaction is highly non-linear, the reduction of $E$ has a stronger effect at lower end-block fractions, which can be seen when comparing Fig. 9c and Fig. 2. In particular, the microphase boundaries shift to lower concentration at low end-block fraction for $E$ of 250,000 as opposed to $E$ of 500,000.

## 4 Conclusions

We have developed a new EF model to efficiently simulate the phase behavior of a system of oppositely charged triblock copolyelectrolytes dissolved in water. This model was validated against FTS-CL of a full, non-approximated model with explicit Coulomb interactions. Additionally, the phase behavior was computed and directly compared with experimental phase behavior which was determined using SAXS. Excellent qualitative agreement was observed between the computational and experimental results both with respect to phase behavior and domain spacing. Phase diagrams with respect to polymer concentration and end-block fraction suggest that polymer concentration can be more efficiently used to select the structure of a phase, which may be of interest in applications since samples can be dehydrated or hydrated to select the structure of the resulting material. Additionally several trends for domain spacing were observed. Generally increasing the end-block fraction increased the domain spacing. The domain spacing also tends to decrease for a given structure with in-

creasing polymer concentration due to reduced swelling by water.

Given the success of our model and computational approach, design principles were determined for how the chemistry of the triblock copolyelectrolytes can be tuned to shift the boundaries on the phase diagram. In particular we looked at chemical incompatibility between end-blocks and mid-blocks, solvent quality of the end-blocks, and charge density. These results provide insight into how the functionality of the copolyelectrolytes can be tuned to yield desired structures of practical use. Also, the success of this study suggests that analogous models could be developed for predicting the phase behavior of more complicated polymer architectures. The model can also be easily extended to include counterions and explore the role of pH through charge asymmetry. The role of a non-uniform dielectric constant could also be incorporated.

## Acknowledgements

This work was supported by the MRSEC Program of the National Science Foundation under Award No. DMR 1121053 to the Materials Research Laboratory at UCSB. We also acknowledge support from the UCSB Center for Scientific Computing: jointly funded by the California Nanosystems Institute, the Materials Research Laboratory (NSF DMR-1121053), Hewlett Packard and NSF CNS-0960316. D.J.A. would also like to thank Dr. Kris Delaney for helpful discussions.

## References

1 C. Tsitsilianis, *Soft Matter*, 2010, **6**, 2372–2388.
2 M. C. Stuparu, A. Khan and C. J. Hawker, *Polym. Chem.*, 2012, **3**, 3033–3044.
3 N. A. Peppas, *Curr. Opin. Colloid In.*, 1997, **2**, 531 – 537.
4 P. Gupta, K. Vermani and S. Garg, *Drug Discov. Today*, 2002, **7**, 569 – 579.
5 A. Bajpai, S. K. Shukla, S. Bhanu and S. Kankane, *Prog. Polym. Sci.*, 2008, **33**, 1088 – 1118.
6 T. R. Hoare and D. S. Kohane, *Polymer*, 2008, **49**, 1993 – 2007.
7 J. A. Hubbell, *Nat. Biotech.*, 1995, **13**, 565–576.
8 J. D. Kretlow, L. Klouda and A. G. Mikos, *Adv. Drug Deliver. Rev.*, 2007, **59**, 263 – 273.
9 S. Khetan and J. A. Burdick, *Soft Matter*, 2011, **7**, 830–838.
10 M. Guvendiren, H. D. Lu and J. A. Burdick, *Soft Matter*, 2012, **8**, 260–272.
11 N. A. Peppas and J. J. Sahlin, *Biomaterials*, 1996, **17**, 1553 – 1561.
12 A. Brzozowska, B. Hofs, A. de Keizer, R. Fokkink, M. A. Cohen Stuart and W. Norde, *Colloid Surfaces A*, 2009, **347**, 146 – 155.
13 S. van der Burgh, R. Fokkink, A. de Keizer and M. . Cohen Stuart, *Colloid and Surfaces A*, 2004, **242**, 167 – 174.
14 H. G. Bungenberg de Jong and H. R. Kruyt, *Proc. Koninkl. Nederland. Akad. Wetenschap.*, 1929, **32**, 849–856.
15 A. Harada and K. Kataoka, *Macromolecules*, 1995, **28**, 5294–5299.
16 A. Harada and K. Kataoka, *Science*, 1999, **283**, 65–67.
17 A. V. Kabanov, T. K. Bronich, V. A. Kabanov, K. Yu and A. Eisenberg, *Macromolecules*, 1996, **29**, 6797–6802.
18 M. A. Cohen Stuart, N. A. M. Besseling and R. G. Fokkink, *Langmuir*, 1998, **14**, 6846–6849.
19 M. Lemmers, J. Sprakel, I. K. Voets, J. van der Gucht and M. A. Cohen Stuart, *Angew. Chem.*, 2010, **122**, 720–723.
20 M. Lemmers, I. K. Voets, M. A. Cohen Stuart and J. van der Gucht, *Soft Matter*, 2011, **7**, 1378–1389.
21 M. Lemmers, E. Spruijt, L. Beun, R. Fokkink, F. Leermakers, G. Portale, M. A. Cohen Stuart and J. van der Gucht, *Soft Matter*, 2012, **8**, 104–117.
22 J. N. Hunt, K. E. Feldman, N. E. Lynd, J. Deek, L. M. Campos, J. M. Spruell, B. M. Hernandez, E. J. Kramer and C. J. Hawker, *Adv. Mater.*, 2011, **23**, 2327–2331.
23 D. V. Krogstad, N. A. Lynd, S.-H. Choi, J. M. Spruell, C. J. Hawker, E. J. Kramer and M. V. Tirrell, *Macromolecules*, 2013, **46**, 1512–1518.
24 M. J. Voorn, *Rel. Trav. Chim. Pay-B*, 1956, **75**, 317–330.
25 J. T. G. Overbeek and M. J. Voorn, *J. Cell. Compar. Physl.*, 1957, **49**, 7.
26 V. Y. Borue and I. Y. Erukhimovich, *Macromolecules*, 1988, **21**, 3240.
27 V. Y. Borue and I. Y. Erukhimovich, *Macromolecules*, 1990, **23**, 3625.
28 A. V. Ermoshkin and M. Olvera de la Cruz, *Macromolecules*, 2003, **36**, 7824–7832.
29 A. Kudlay and M. Olvera de la Cruz, *J. Chem. Phys.*, 2004, **120**, 404.
30 A. Kudlay, A. V. Ermoshkin and M. Olvera de la Cruz, *Macromolecules*, 2004, **37**, 9231.
31 M. Castelnovo and J.-F. Joanny, *Euro. Phys. J. E*, 2001, **6**, 377–386.
32 P. M. Biesheuvel and M. A. Cohen Stuart, *Langmuir*, 2004, **20**, 4764–4770.
33 Z. Ou and M. Muthukumar, *J. Chem. Phys.*, 2006, **124**, 154902.
34 M. A. Trejo-Ramos, F. Tristán, J.-L. Menchaca, E. Pérez and M. Chávez-Páez, *J. Chem. Phys.*, 2007, **126**, 014901.
35 Y. Hayashi, M. Ullner and P. Linse, *J. Chem. Phys.*, 2002, **116**, 6836–6845.
36 Y. Hayashi, M. Ullner and P. Linse, *J. Phys. Chem. B*, 2003, **107**, 8198–8207.
37 Y. Hayashi, M. Ullner and P. Linse, *J. Phys. Chem. B*, 2004, **108**, 15266–15277.
38 C. Narambuena, E. Leiva, M. Chvez-Pez and E. Prez, *Polymer*, 2010, **51**, 3293 – 3302.
39 R. S. Dias, P. Linse and A. A. C. C. Pais, *J. Comput. Chem.*, 2011, **32**, 2697–2707.
40 A. A. Lazutin, A. N. Semenov and V. V. Vasilevskaya, *Macromol. Theor. Simul.*, 2012, **21**, 328–339.
41 R. G. Winkler, M. O. Steinhauser and P. Reineker, *Phys. Rev. E*, 2002, **66**, 021802.
42 Y. O. Popov, J. Lee and G. H. Fredrickson, *J. Poly. Sci. B*, 2007, **45**, 3223–3230.
43 J. Lee, Y. O. Popov and G. H. Fredrickson, *J. Chem. Phys.*, 2008, **128**, 224908.
44 R. A. Riggleman, R. Kumar and G. H. Fredrickson, *J. Chem. Phys.*, 2012, **136**, 024903.
45 V. Ganesan and G. Fredrickson, *Europhys. Lett.*, 2001, **55**, 814–820.
46 G. H. Fredrickson, V. Ganesan and F. Drolet, *Macromolecules*, 2002, **35**, 16–39.
47 M. Castelnovo and J. F. Joanny, *Macromolecules*, 2002, **35**, 4531–4538.
48 N. P. Shusharina, E. B. Zhulina, A. V. Dobrynin and M. Rubinstein, *Macromolecules*, 2005, **38**, 8870–8881.
49 J. Jeon and A. V. Dobrynin, *Macromolecules*, 2005, **38**, 5300–5312.
50 J. Ziebarth and Y. Wang, *J. Phys. Chem. B*, 2010, **114**, 6225–6232.
51 J. Feng and E. Ruckenstein, *J. Chem. Phys.*, 2006, **124**, 124913.
52 C. E. Sing, J. W. Zwanikken and M. O. de la Cruz, *Phys. Rev. Lett.*, 2013, **111**, 168303.
53 C. E. Sing, J. W. Zwanikken and M. Olvera de la Cruz, *ACS Macro Letters*, 2013, **2**, 1042–1046.

54 C. E. Sing, J. W. Zwanikken and M. Olvera de la Cruz, *Nat Mater*, 2014, **7**, 694–698.

55 M. Doi and S. Edwards, *The Theory of Polymer Dynamics*, Oxford University Press, New York, 1986.

56 Z.-G. Wang, *Phys. Rev. E*, 2010, **81**, 021501.

57 S. F. Edwards, *P. Phys. Soc.*, 1965, **85**, 613.

58 B. H. Zimm, W. H. Stockmayer and M. Fixman, *J. Chem. Phys.*, 1953, **21**, 1716–1723.

59 G. H. Fredrickson, *The Equilibrium Theory of Inhomogeneous Polymers*, Oxford University Press, New York, 2006.

60 M. W. Matsen, *J. of Phys.: Condens. Matter*, 2002, **14**, R21.

61 M. W. Matsen, *Self-Consistent Field Theory and Its Applications*, Wiley-VCH, Weinheim, 2006.

62 E. M. Lennon, K. Katsov and G. H. Fredrickson, *Phys. Rev. Lett.*, 2008, **101**, 138302.

63 R. A. Riggleman and G. H. Fredrickson, *J. Chem. Phys.*, 2010, **132**, 024104.

64 Z. Mester, N. A. Lynd and G. H. Fredrickson, *Soft Matter*, 2013, **9**, 11288–11294.

65 J.-L. Barrat, G. H. Fredrickson and S. W. Sides, *J. Phys. Chem. B*, 2005, **109**, 6694–6700.

66 A. Ranjan, J. Qin and D. C. Morse, *Macromolecules*, 2008, **41**, 942–954.

67 A. Z. Panagiotopoulos, *Molecular Physics*, 1987, **61**, 813–826.

68 A. Panagiotopoulos, N. Quirke, M. Stapleton and D. Tildesley, *Molecular Physics*, 1988, **63**, 527–545.

69 K. Ø. Rasmussen and G. Kalosakas, *J. Polym. Sci., Part B: Polym. Phys.*, 2002, **40**, 1777–1783.

70 G. Tzeremes, K. Ø. Rasmussen, T. Lookman and A. Saxena, *Phys. Rev. E*, 2002, **65**, 041806.

71 D. J. Audus, K. T. Delaney, H. D. Ceniceros and G. H. Fredrickson, *Macromolecules*, 2013, **46**, 8383–8391.

72 D. V. Krogstad, S.-H. Choi, N. A. Lynd, D. J. Audus, S. L. Perry, J. D. Gopez, C. J. Hawker, E. J. Kramer and M. V. Tirrell, *J. Phys. Chem. B*, 2014, **118**, 13011–13018.

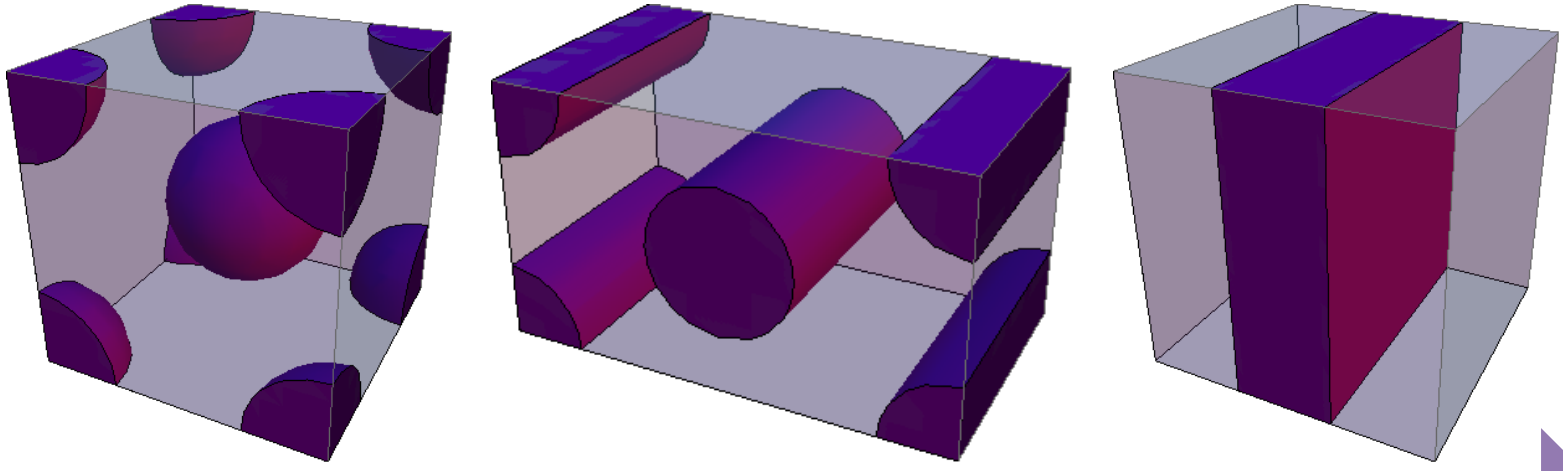

Increasing polymer concentration

Text for graphical abstract:

We explore the phase behavior of responsive hydrogels composed of oppositely charged triblock polymers in aqueous solution using a new embedded fluctuation model coupled with self-consistent field theory simulations.